NMR in Biomedicine

WILEY

NMR IN BIOMEDICINE

REVIEW ARTICLE

Breaking the Limits of Low-Field MRI: Deep Learning Approaches to Image Enhancement

Xuanyu Zhu[1] | Yun Shang[2] | Hsin-Jung Yang[3] | Lei Yang[1] | Ziyang Long[3,4] | Hongfu Sun[5] | Fuchun Lin[1] | Xin Zhou[1] | Hui Han[1]

[1]State Key Laboratory of Magnetic Spectroscopy and Imaging, National Centre for Magnetic Resonance in Wuhan, Wuhan Institute of Physics and Mathematics, Innovation Academy for Precision Measurement Science and Technology, Chinese Academy of Sciences, Wuhan, China | [2]Department of Radiology, Weill Cornell Medicine, Cornell University, New York, New York, USA | [3]Cedars-Sinai Medical Center, Biomedical Imaging Research Institute, USA | [4]Department of Bioengineering, University of California, Los Angeles, Los Angeles, California, USA | [5]School of Engineering, The University of Newcastle, Newcastle, New South Wales, Australia

Correspondence: Xin Zhou (xinzhou@apm.ac.cn) | Hui Han (huihan@apm.ac.cn)

Received: 2 October 2025 | **Revised:** 8 February 2026 | **Accepted:** 17 March 2026

Keywords: deep learning | image denoising | low-field MRI | super-resolution

ABSTRACT

Low-field magnetic resonance imaging (LF-MRI) has emerged as a transformative technology, offering portable and cost-effective solutions for medical imaging in resource-limited settings. However, LF-MRI systems face inherent challenges, including low signal-to-noise ratio (SNR) and reduced spatial resolution, which can compromise diagnostic accuracy. To systematically address these fundamental limitations, which involve complex, nonlinear image transformations, deep learning (DL) presents a powerful solution due to its proven capability in learning such mappings from data. This review explores the pivotal role of DL techniques in overcoming these limitations, focusing on two critical applications: denoising and super-resolution. Recent advancements in DL architectures—such as U-Net, generative adversarial networks (GANs), and diffusion models (DMs)—have demonstrated remarkable success in enhancing LF-MRI image quality. For denoising, supervised models like U-Net and denoising auto-encoders (DAEs) effectively suppress noise while preserving anatomical details, while unsupervised approaches (e.g., Cycle-GANs) leverage unpaired datasets to bridge the gap between low-field (LF) and high-field (HF) MRI. In super-resolution, DL models like 3D U-Net and residual channel attention networks (RCANs) reconstruct high-resolution images from LF inputs, enabling finer detail visualization for clinical diagnostics. Key findings highlight the superiority of DL over conventional iterative methods in adaptability, robustness, and real-time performance. However, challenges persist, including data dependency, computational costs, and limited interpretability. Innovations such as diffusion-driven neural representations and dual-acquisition 3D super-resolution further push the boundaries of LF-MRI quality. This review underscores DL's potential to democratize MRI access, particularly in low-resource regions, while outlining future directions: improving generalization, reducing training data requirements, and integrating postprocessing pipelines. By directly tackling the key barriers of image quality, DL-enhanced LF-MRI is poised to make a significant impact in clinical scenarios where accessibility and speed are paramount, such as point-of-care diagnostics and emergency clinic, thereby helping bridge global healthcare disparities.

1 | Introduction

1.1 | History of Low-Field and Portable MRI: Utilities and Limitations

For several years, low-field magnetic resonance imaging (LF-MRI) system has been at the forefront of medical imaging, providing a noninvasive method to explore the intricate structures within the human body [1–3]. The root of LF-MRI could trace back to early MRI research concepts, gaining traction with advancements in magnet design [4–7]. These systems target environments traditionally lacking advanced medical imaging capabilities by reducing magnetic field strength to below 1T, minimizing infrastructure requirements and enabling easier installation and operation in decentralized medical settings [8, 9]. LF-MRI could fill the gap that conventional MRI systems face as insufficient clinical requirements and low flexibility [10, 11]. For instance, it could be equipped in low- and middle-income regions, where MRI implementations could not satisfy the need of in the local clinic [12, 13]. Many research works regarding the LF-MRI system and imaging quality enhancement had emerged.

Based on magnetic field strength, LF-MRI systems can be further categorized into low field (0.1–1 Tesla) and ultra-low field (< 0.1 Tesla) MRI. Typical LF scanners include the 0.5T Synaptive Evry [14, 15] intraoperative scanner and the 0.55T Siemens Magnetom Free. Max [16, 17]. One well-known ultra-low field scanner is the 0.064T Hyperfine Swoop head scanner [18–20], which has been adopted by many groups globally. Additionally, several research initiatives have developed custom-designed systems, such as the 0.05T permanent dipole system at Chongqing University [21] and the 0.055T system at Hong Kong University [22, 23]. The clinical application of these LF portable MRI represents a significant advancement in making imaging more accessible. Not only do these compact systems facilitate rapid deployment in diverse clinical and field settings, but they also meet special critical needs (e.g., pediatric scan) in immediate care scenarios such as emergency medicine and disaster response, ensuring timely access to diagnostic information [6, 24, 25]. However, LF-MRI systems often experience significant noise, primarily due to the inherently lower signal-to-noise ratio (SNR) compared to high-field MRI (HF-MRI) systems [26]. This noise originates from various sources, including the electronic components of the MRI scanner (e.g., the preamplifier noise [27, 28]), thermal noise (e.g., Johnson-Nyquist Noise, majorly form the receiver coil [29–31]), and the magnetic environment itself (i.e., electromagnetic interference, EMI [32–35]). The lower magnetic field strength contributes to weaker signal emissions from tissues, making it difficult to distinguish between true signals and noise. Resolution is another limitation of LF-MRI, because weaker B_0 reduced SNR and forced larger voxels with longer scan periods. Thus, resolution recovery became the second key aspect focusing on the image quality enhancement. It is essential for evaluating intricate anatomical details and small pathological changes and reduce the processing time [36].

Many conventional iterative methods were developed to tackle these problems. Examples to improve resolution could be found in the applications of sparse sampling [37] or interpolation [10, 38, 39]. Other techniques focusing SNR improvement could also be witnessed in denoising methods (e.g., signal-image domain filtering [40]) or tissue-wise segmentation toolbox (e.g., the FMRIB automated toolbox FSL-FAST [26]). However, these approaches often face significant limitations as excessive parameter tuning, which increased computational demands and led to variability in the results. Additionally, conventional iterative methods can be sensitive to noise and artifacts inherent. These methods are also "capped" in terms of performance, and their improvement is limited compared to DL. These disadvantages highlight the need for more robust and efficient approaches, such as those derived from deep learning, to advance LF-MRI technology and improve diagnostic outcomes.

1.2 | DL-Based Models and LF-MRI

The resurgence of low-field MR imaging in recent years has largely been driven by the advances in DL techniques. Learning-based models, particularly neural networks (e.g., U-net and fully convolutional networks [41–43]), are instrumental in enhancing image quality and diagnostics. Generally, various DL applications exploit prior anatomical knowledge from extensive datasets and overcome SNR limitations and facilitating efficient. Owing to the nonlinearity, learning-based methods increased the complexity and the stability of the computation and avoid the limitation as being a single-layer model. In addition to conventional supervised networks, typical unsupervised architectures such as generative adversarial networks (GANs) [44] and extensions (e.g., conditional GANs [45, 46] and Cycle-GANs [47–49]) have been developed, which reduced the need of paired images between LF and HF. Further unsupervised structures, for example, diffusion models (DMs) [50] and transformer learning [51], delivered enhanced image detail and fidelity. Depending on the application, learning-based structures can be tailored to meet specific training destinations and carefully captured training datasets where developments are needed. Figure 1 exhibits a visual comparison in the case of super-resolution. Detailed structures of these learning structures will be discussed in the following sections.

The foundation that guarantees the performance of DL-based models is the large scale and precisely designed training data, which benefit the network structures to learn patterns and reveal characteristics. Regarding the two main perspectives of LF enhancement, different learning-based models were developed and delivered many construction models. Datasets of denoising-based NNs are generated with pairs of noise-added (as inputs) and clean data (as labels or ground truth). Through this strictly supervised learning process, the networks learn to identify and suppress noise patterns while preserving essential anatomical details, and the final output will be more accurate with a higher SNR [52–57]. One typical noise comes from electromagnetic interference (EMI). EMI signals fluctuate due to nearby sources and the human body acting as an antenna [58]. Several training-set designs approach this issue by identifying and isolating interference patterns from the true imaging signals.

Considering the super-resolution training, the dataset was generally defined as the direct reconstruction from lower- to higher-resolution images. Well-trained models can improve the detail and sharpness in MRI scans, making them more comparable to those acquired from HF systems. The capability of enhancing image quality is particularly important for applications requiring precise anatomical visualization. The studies [59–63], such as in neuroimaging and oncological assessments, revealed that every additional detail can inform a more nuanced understanding of disease progression and response to treatment. However, learning-based models in low-field MRI face general challenges such as data dependency, high computational demands, lack of interpretability, and difficulties with generalization and artifact sensitivity, limiting their clinical application.

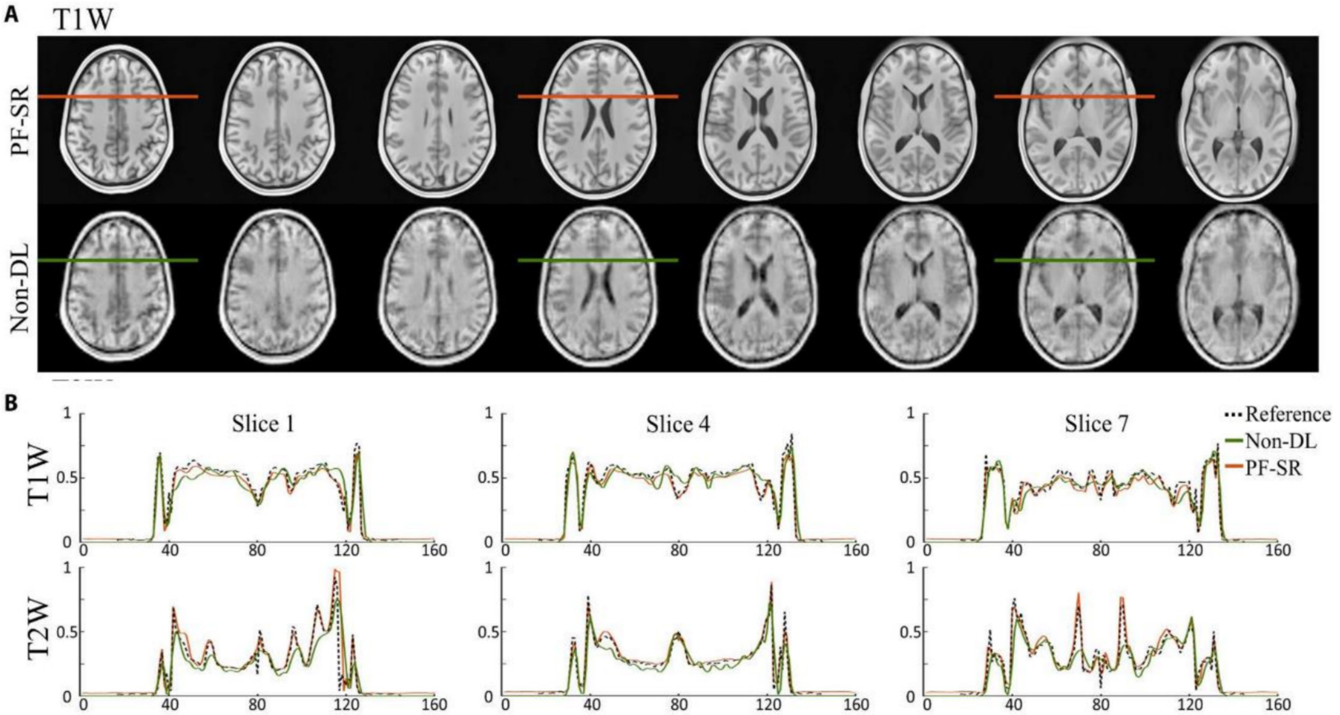

FIGURE 1 | Comparison between proposed DL method (partial Fourier super-resolution model) and traditional iterative method on 3D synthetic brain with noise [23]. LF data were simulated from HCP S1200 dataset (3T Siemens "Connectome Skyra" at WashU), including 3D T1W MPRAGE and T2W SPACE, both with 0.7 mm isotropic resolution. The visual illustration is performed on (A) T1W image and (B) intensity line profiles of both T1W and T2W data.

TABLE 1 | General comparison of deep learning–based and conventional algorithms in low-field MRI.

Feature	Deep learning–based methods	Conventional algorithms
Performance	Superior performance in image reconstruction, denoising, and classification through learned patterns	Performs well in basic tasks but limited in complex situations
Data requirements	Require large-labeled datasets but can generalize well with enough data	Operate effectively on smaller datasets, less dependent on vast amounts of data
Adaptability	Highly adaptable to different tasks with fine-tuning capabilities	Specifically designed for targeted problems, less flexible and extendable
Robustness	Greater robustness to noise and artifacts by learning inherent data features	More vulnerable to image noise and artifacts, may require additional corrections
Real-time capability	Enhanced real-time capabilities with optimized models or hardware	Efficient in real-time applications due to simpler processing
Automated feature learning	Automatically learns and extracts relevant features, reducing the need for manual input	Relies on predefined features; manual feature engineering required
Generalization to new data	Better generalization to unseen data with appropriate training and validation	May struggle with generalization to new or different dataset variations

Table 1 listed the general advantages of DL-based methods compared to conventional iterative solutions.

1.3 | Outline of This Review Paper

This review has the following structure. First, the advancements in denoising techniques utilized in LF-MRI will be discussed, focusing on how various DL methodologies enhance image quality by effectively reducing noise levels. Next, the super-resolution approaches will be introduced, enabling the acquisition of clearer and more detailed images that are essential for accurate diagnostics. This review paper will analyze several manuscripts to introduce the various network structures employed in this context, detailing their respective methodologies and implementations. Additionally, it will cover essential aspects of data preparation and postprocessing techniques that enhance image quality.

2 | Denoising Models via Supervised and Unsupervised Learnings

DL models, particularly convolutional neural networks (CNNs), have been highly effective in addressing this issue through advanced denoising techniques. Different research works have investigated multiple networks, which were trained on public datasets (e.g., Human Connectome Project) or typically designed biostructure or tissues (e.g., fetal body) to recognize and filter out noise while preserving essential image details.

2.1 | Supervised Denoising: U-Net Architecture and Extensions

A key CNN architecture applied in denoising is U-Net [41], known for its effective encoder-decoder structure. The encoder consists of convolutional layers followed by pooling layers, which compress the image while extracting important features. The decoder uses transposed convolutions to up-sample the feature maps and reconstruct the image. U-Net incorporates skip connections that link corresponding layers in the encoder and decoder sections, preserving spatial information and fine details. This design enhances the network's ability to filter out noise while maintaining crucial anatomical details. Thus, several HF-MRI denoising experiments [64–68] selected U-Net for improving image quality and diagnostic accuracy. Inspired by the successful implementation, LF-MRI reconstruction has also applied end-to-end training using U-Net.

A classical 3D isotropic U-Net architecture has been utilized with the mapping of two identical-size input and output cubes [69]. The U-net–based architecture in Figure 2a incorporates a bottleneck block [72, 73] that designed to connect the contracting and expanding paths. This bottleneck block is defined by the following three hyperparameters: the input filter, the number of shrinking layers, and the up-sampling scaling factor. For this implementation, a scaling factor of ($k=4$) was used, in which the network first down-samples the initial dimensions to become isotropic and then performs isotropic down- and up-sampling. Training was adjusted via the loss function pixel-wised mean squared error (MSE) [41]. The central methodological innovation is a probabilistic decimation

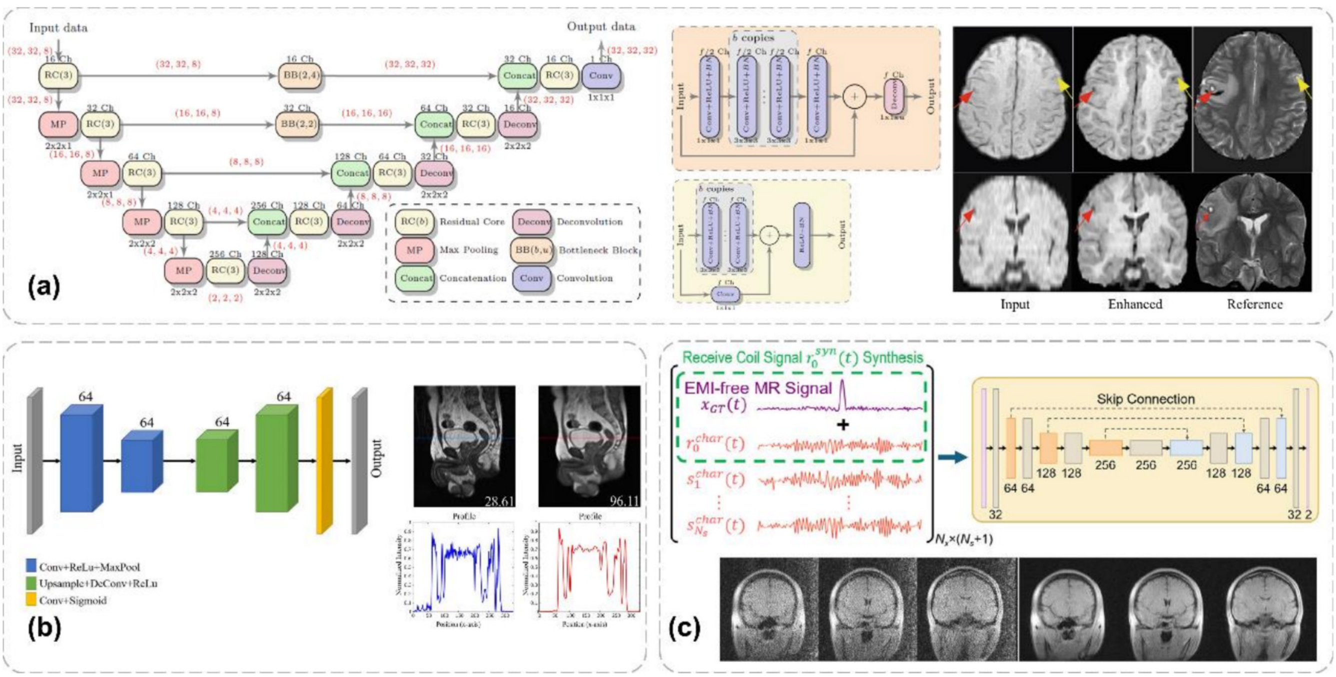

FIGURE 2 | (a) The diagram of anisotropic U-net with the illustration of bottleneck block and residual core [69], and results from image quality transfer (IQT) prediction on the LF epileptic patient data (0.36T MagSense 360 MRI System scanner, nonisotropic voxel size of 0.9 mm × 0.9 mm × 7.2 mm, including 6.0-mm slice thickness and 1.2 mm gaps). (b) Denoising auto encoder architecture [70], with image reconstruction from the 0.35T images (MR-Linac, MRIdian, ViewRay Inc., Oakwood Village, OH, USA). SNR measurement and profile lines are also exhibited. (c) A residual U-Net model is trained using 3D T1W image detected during the EMI signal characterization [71], on a home-built shielding-free 0.055T brain MRI scanner (gradient-recalled echo, TR/TE = 52/13 ms, flip angle = 40°, BW = 6.25 kHz, FOV = 250 mm × 250 mm × 320 mm, acquisition matrix = 128 × 128 × 32, and NEX = 2).

model designed to stabilize image quality transfer (IQT) training and improve low-field MRI reconstruction quality (e.g., on pediatric epilepsy data). However, the network was trained through T1-weighted images (Siemens Connectome scanner) from Human Connectome Project (HCP) dataset and make inference using the same ones, hence the diversity of the validation became the main disadvantage. A variation of conventional U-net was developed by Armando Garcia Hernandez et al. [70], known as the denoising auto-encoder (DAE). DAE was also stablished by the idea of U-net structure, without the layer concatenations and skip connection, shown in Figure 2b. The 2D pelvic dataset was acquired from Siemens 1.5T scanner and utilized to train the DAE model, with the Rician noise added. Loss function is customized to enforce the anatomical detection with a total variation (TV) penalty alongside MSE. The well-trained model illustrated a clinical transfer learning strategy that improved the real-world application from 0.35T MR-Linac (MRIdian, ViewRay Inc., Oakwood Village, OH, USA). In addition, another DAE contribution by Ethan MacDonald et al. [74] exhibited the effective synthesis of high-quality (high-SNR, high-resolution) MRI from low-field, low-SNR inputs. The training was implemented using IXI database [75] containing 70 brain subjects acquired at 3T. This DAE architecture was implemented onto the seven-layer U-net structure, with the results that indicated DAE performed well with normally distributed noise. The other denoising study from David Schote et al. [76] also established a cascaded network to solve the B_0 inhomogeneity and distortion correction, which employed the U-net architecture as the denoising section. Training data comprised retrospectively simulated LF knee MRI at $B_0 \sim 50$mT.

EMI becomes another factor of the noise of LF-MRI system. Yujiao Zhao et al. [71] propose Deep-DSP, an architecture built from a residual U-net [73] that directly predicts EMI-free MR signals from raw data via an EMI characterization scheme from 3d-FSE acquisition. Deep-DSP enabled robust RF elimination for portable MRI. The processing pipeline is shown in Figure 2c. The model was trained using synthetic MRI data (created by adding simulated EMI-free signals to EMI-only MRI data) and EMI sensing coil data. The loss function used was L1 loss, optimized using the Adam optimizer. Evaluation data involved simulated phantoms and in vivo acquisitions. Simultaneous subjects were generated via the similar noise-adding method of training datasets. Experimental in vivo brain data were acquired from multiple EMI sensing coils on a home-built shielding-free 0.055T brain MRI scanner and a 1.5T whole-body scanner (with incomplete shielding).

Expanding upon the techniques of U-Net, diverse supervised learning architectures are explored for LF-MRI denoising. N. Koonjoo et al. [77] explore AUTOMAP, which featured two fully connected layers and multiple convolutional layers with rectifier nonlinearities, as Figure 3a shows. This work contributes the neural network directly to raw k-space data from extremely low-field MRI systems (6.5 and 47 mT). Its key innovation lies in operating in the sensor domain rather than the image domain, enabling superior noise suppression and

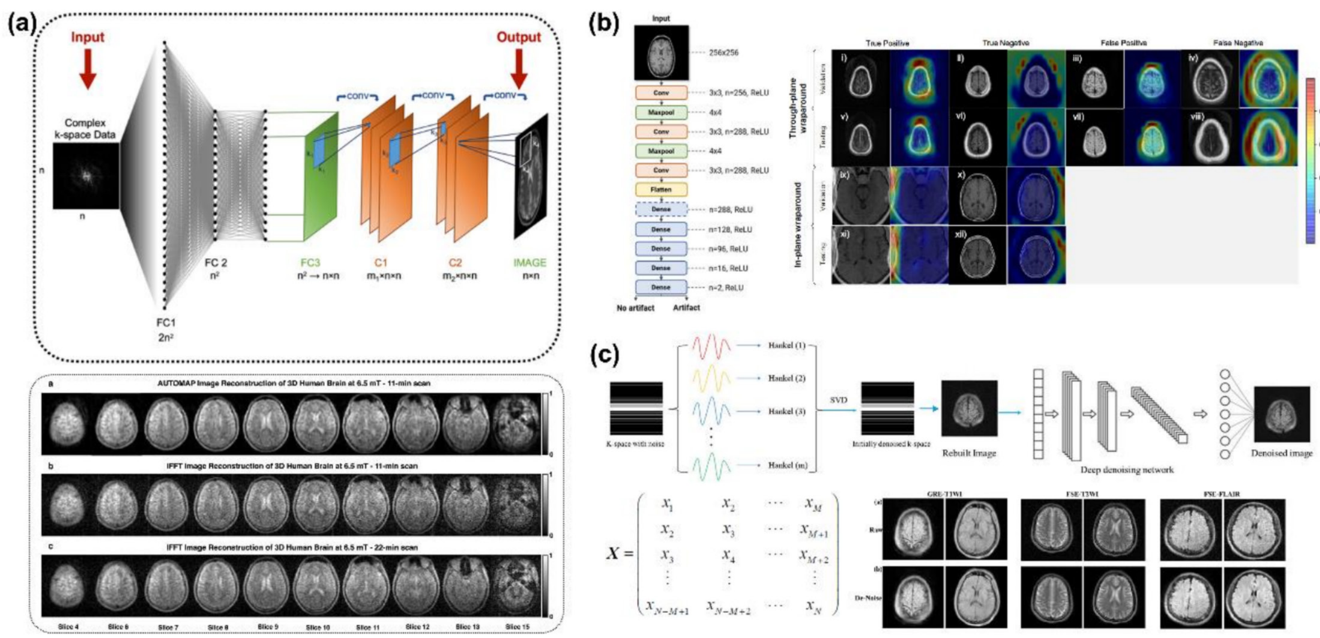

FIGURE 3 | (a) AUTOMAP neural network architecture and AUTOMAP [77] reconstruction at a customized 6.5mT scanner via a 3D human head dataset—an 11-min 3D acquisition (3D b-SSFP sequence with TR = 31 ms, matrix size = 64 × 75 × 15, spatial resolution = 2.5 mm × 3.5 mm × 8 mm,), compared with traditional IFFT (in both 11- and 22-min scan). (b) Architectures of the ArtifactID [78]: 2D convolutional neural networks, and the representative Grad-CAM heatmaps localized both types of wrap-around artifacts across TP, TN, FP, and FN samples from the validation and test sets, acquired from a 0.36T MagSense 360 (Mindray, China) open MRI scanner (parameters: TE = 15 ms, TR = 569–814 ms, slice thickness = 4–6 mm, matrix size varied from 192 × 192 to 512 × 512). (c) Denoising process for ULF MRI [21] via home-built 54mT scanner. The discrete time-domain signals can be initially structured into a Hankel matrix using the linear predictability principle. Results of Image enhancement include GRE-T1WI, FSE-T2WI, and FSE-FLAIR (Acquisition parameters for each sequence could be viewed in original manuscript).

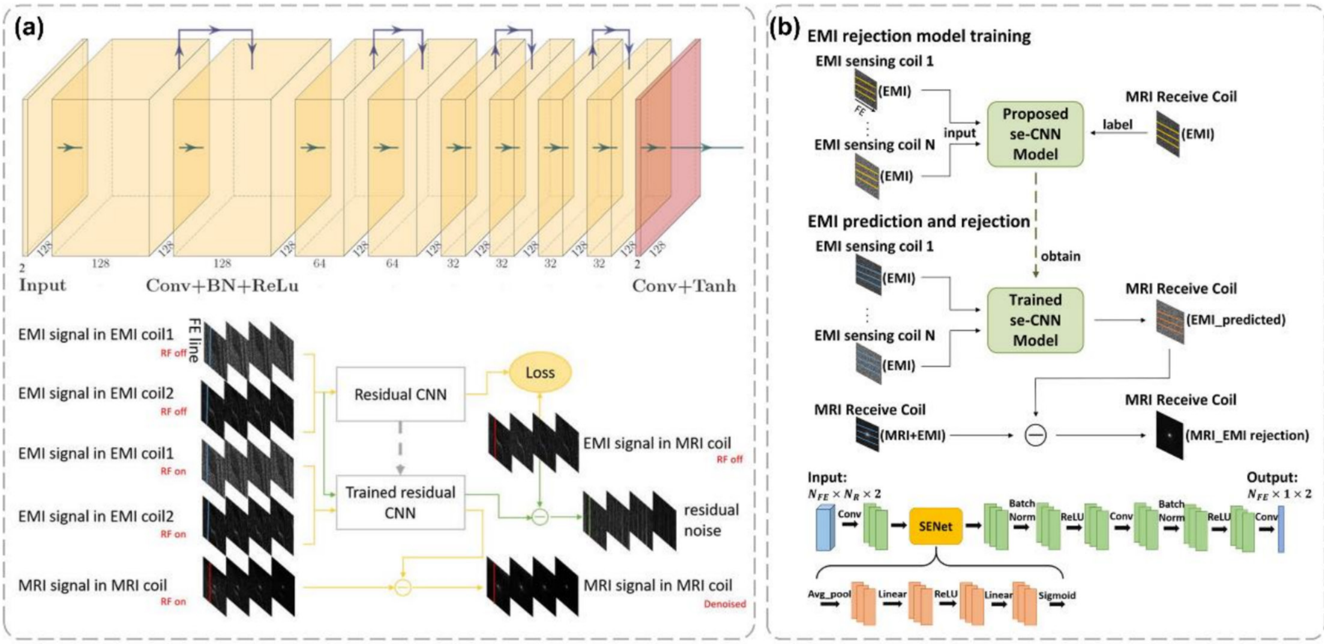

FIGURE 4 | (a) Dual-step algorithm for shielding-free LF-MRI, with a combination of four-bloac residual CNN and a triple-generator WGAN (TWGAN) [80]. (b) Architectures of the SENet attention mechanism incorporated within a three-layer CNN [81].

elimination of structured artifacts (e.g., spike noise) by learning a transformation between low-dimensional manifolds. Data were acquired using balanced SSFP sequences at a customized 6.5 mT scanner for both 2D phantoms and 3D in vivo brain imaging with adjustments in acquisition settings. The training datasets comprised 51,000 2D brain images from the HCP dataset and included synthetic data to improve robustness against artifacts. The training utilized RMSProp optimization with L1 loss penalties, focusing on *k*-space corrupted data to produce noise-free images, evaluated via metrics like RMSE and SSIM. Marina Manso Jimeno et al. developed the ArtifactID, a separate binary classification model [78], to identify wrap-around and Gibbs ringing artifacts in LF-MRI. Two datasets—one from the IXI database (Philips 1.5T, GE 1.5T, Philips 3T) and another from a LF-MRI scanner (0.36T MagSense 360 open MRI scanner)—were trained with the simulated artifacts. The key innovation of ArtifactID is the design of the modular, artifact-specific framework. This design integrates gradient-weighted class activation mapping (Grad-CAM) to provide explainable AI, visually localizing artifacts within the images. Grad-CAM visualizations [79] helped analyze model predictions and classify artifact occurrences, with the training process accounting for imbalances in artifact representation. The general structure of ArtifactID is viewed in Figure 3b. Another study conducted by Fanqin Meng et al. [21] established a two-step cascaded network that combines fast imaging from *k*-space with denoising, the pipeline is shown in Figure 3c. Its primary contribution is demonstrating a practical, sequential processing workflow that accelerated imaging with a supervised DL denoiser to improve the SNR and visual quality of ULF brain scans across multiple contrast weightings (T1, T2, and FLAIR). For fast imaging, the *k*-space data are undersampled and structured into a Hankel matrix, allowing low-rank matrix recovery via singular value decomposition (SVD) for initial noise reduction. For denoising, transfer learning was implemented and trained on high-quality 1.5T MRI images, sourced from Chongqing University's hospital. Fine-tuning was processed using ULF MRI data acquired by the home-built 54mT scanner.

Beyond the U-net variants introduced earlier for EMI suppression, other CNN-based frameworks have also shown promising results in tackling EMI under different system configurations and noise environments. Yang Hu et al. [80] propose a dual-step denoising algorithm (DDA) for shielding-free LF-MRI, viewed in Figure 4a. The first step uses a four-block residual CNN to map EMI sensor signals to MRI coil noise. The second step employs a triple-generator WGAN (TWGAN) for refinement. Training data consist of *k*-space FE lines from a homemade shielding-free 0.11T scanner, with a dataset of 150 clean-noise pairs constructed by adding scaled residual noise to shielded-room acquisitions. Evaluation metrics include SSIM and NRSS (no-reference structural sharpness). TWGAN contributes to the secondary denoising refinement and enables superior performance and generalizability on low-field (0.11T) and ultra-low-field (0.055T) MRI data where hardware shielding is absent. Another EMI-rejection study investigated by Rongsheng Lu et al. [81] proposes a three-layer convolutional neural network (CNN) incorporating a SENet attention mechanism (se-CNN) shown in Figure 4b. The study developed a hardware-optimized method for active EMI rejection via a multi-indicator coil selection strategy. The SENet-CNN network achieved accelerated training for ~2 min. Data consist of EMI noise signals synchronously acquired from five optimized sensing coils and the main MRI receive coil on a 50 mT portable scanner. The model is trained on the *k*-space data pairs to map noise relationships with/without EMI. Evaluation employs SNR and interference suppression rate to quantify denoising performance and artifact reduction in phantom and in vivo human leg images.

2.2 | Self-Supervised Denoising: GAN-Based Networks, DMs, and Extension

Inspired by success in LF-MRI via conventional CNN backbones (e.g., U-net), GANs offer a complementary approach to enhancing image quality [44]. GANs could be visually considered as the parallel operation of two neural networks—the generator and the discriminator—that work in tandem to produce high-quality images from low-quality inputs. The generator creates images by learning from training data, while the discriminator evaluates the authenticity of these images, providing in-time feedback that improves the generator's output during the duration. Conditional GAN (cGAN) [45] introduced extra information, like class labels, to guide the generation process and produced more targeted outputs.

A GAN-based model for the LoHiResGAN model [19], which involved ResNet [73] components into 3D cGAN backbones, is designed for translating LF-MRI images to HF quality. The model evaluates its performance on data collected from 92 healthy individuals scanned at Monash Biomedical Imaging using both the Hyperfine Swoop (64mT) and Siemens Biograph mMR (3T) imaging systems. Empirical evaluations demonstrated that integrating ResNet blocks significantly contributed to translating LF images effectively with clear anatomical detail recovery. The study also introduced the structural similarity index measure (SSIM) as an additional loss function, alongside mean absolute error (MAE) and binary cross-entropy (BCE) losses.

Instead of cGAN, which requires paired training, Cycle-GAN [47] became another extension that facilitates image-to-image translation using unpaired datasets. The network comprises two generators and two discriminators; one generator produces synthetic denoised images, while the second regenerates the original noisy image. The training was criticized with two loss functions: adversarial loss and cycle consistency loss. In a recent study [48], the entire Cycle-GAN architecture was implemented to improve the quality of LF (64mT, Hyperfine) MRI images by translating them to resemble HF (1.5T, GE Signa HDxt) resolutions. The main contribution and innovation of Cycle-GAN architecture lies in the unpaired image datasets that were matched by radiologists to ensure similarity in brain structures. The process involved a three-step workflow: deformable registration for unpaired images, the Cycle-GAN training, and multimodalities evaluation using

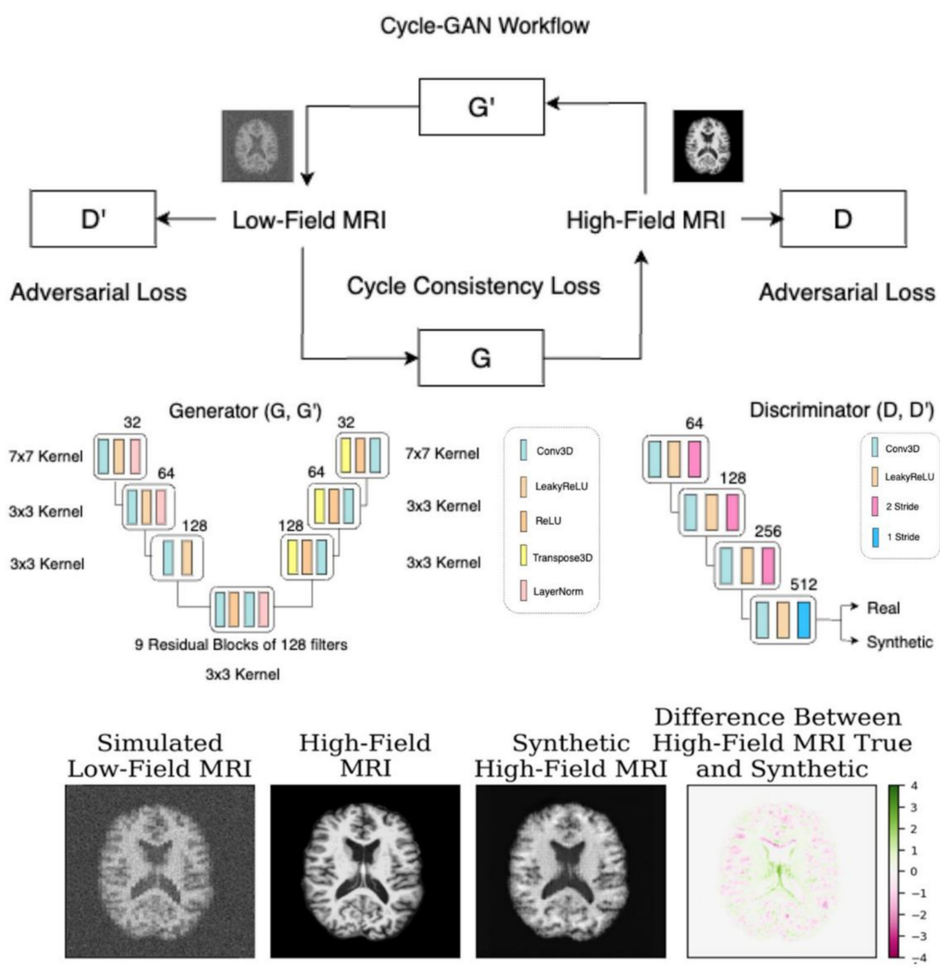

FIGURE 5 | Cycle-GAN workflow in LF-MRI denoising [49] with two generators and corresponding discriminators. G generates a HF-MRI from the LF-MRI and G′ generates the LF-MRI back from the generated HF. Cycle-GAN predictions and different maps to the HF MRI is displayed. Test data are acquired from Open Access Series of Imaging Studies (OASIS-3) database (3T T1W, 1 mm × 1 mm × 1 mm). LF data are simulated to 1.5 mm × 1.5 mm × 1.5 mm with Rician noise, to emulate a low SNR of 70mT.

different combinations of deformable registration and GAN (conventional GAN or Cycle-GAN). Another cycle-GAN model was introduced by Fernando et al. [49] and trained using the OASIS-3 database [82]. The network architecture is demonstrated in Figure 5. The main contribution of the network is super-resolving simulated low-field (70mT) MRI scans to high-field (3T) quality without requiring paired training data.

Differing from GANs that generate data in one step, DMs [83] are a class of generative models used to create data through

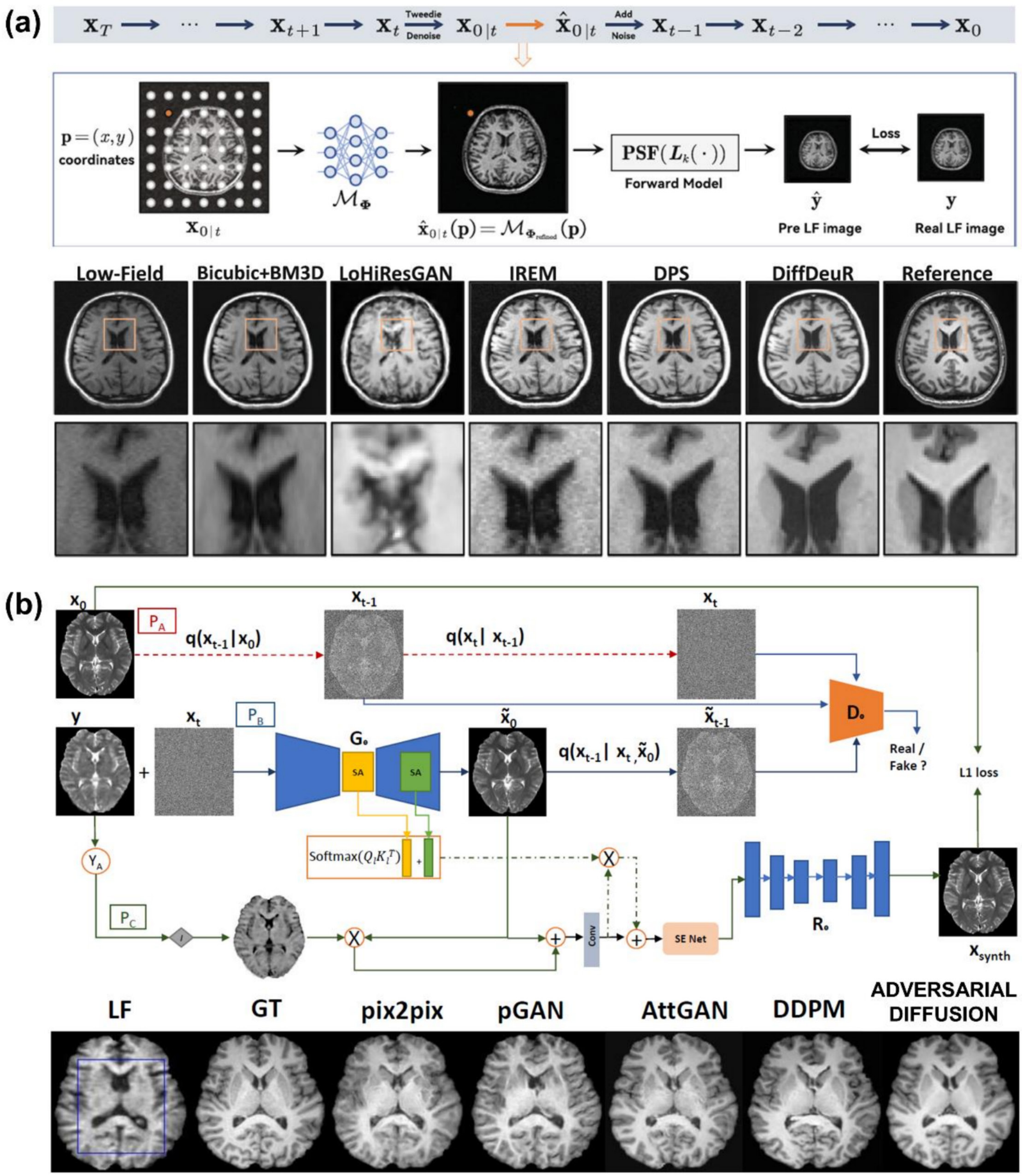

FIGURE 6 | (a) Overview of the proposed DiffDeuR [86] and comparison on one clinical sample of the in vivo LF MRI data (0.2T MR scanner, resolution 1 mm × 1 mm, layer thickness 6 mm). (b) Overview of the proposed architecture consists of diffusive module [90] (with forward diffusion process [P_A], reverse diffusion process [P_B], and attention-guided nondiffusive process [P_C]) with the comparison of the synthesized HF MRI contrasts, LF experiment data were acquired using 64mT Hyperfine Swoop system.

a process that systematically refines noise into structured, reconstructed outputs. This process is formalized in the denoising diffusion probabilistic model (DDPM) [84, 85], which incorporates a Markov chain to gradually add noise during training.

Building on these principles, the proposed DiffDeuR (diffusion-driven neural representation) [86] decomposes the enhancement challenge into two subproblems (e.g., data consistency and prior knowledge) and solved iteratively using a combined DM (specifically the score-based "VE-SDE" model [87]) and implicit neural representation (INR) [88, 89]. The pipeline is shown in Figure 6a. Validation experiments utilized T1-weighted LF data collected from a 0.2T MR scanner and compared it against a HF reference from a 3T uMR 790 MRI scanner. DiffDeuR demonstrates the key contribution to an unsupervised, zero-shot training scheme without requiring paired low-field/high-field training data. In addition, Sanuwani et al. investigated an architecture [90] that features an Adversarial Diffusive Module that employs a 2D GANarchitecture, shown in Figure 6b. This study is the first that contributes a novel adversarial diffusion-based image translation framework to synthesize diagnostic-quality high-field (3T) MRI from ultra-low-field (64mT) scans. An attention-guided refinement module enhances high-level features. Crucially, the model is trained and validated on paired, real 64mT–3T brain MRI data (T1-w, T2-w, FLAIR) from healthy subjects. The architecture is based on a U-Net design integrated with ResNet components, facilitating robust feature extraction and image reconstruction [91]. Experiments used paired LF and HF images collected from Hyperfine Swoop (64mT) and Siemens Biograph mMR 3T imaging systems.

3 | DL-Based Methods in Super-Resolution

Building on the challenges of low spatial resolution in LF-MRI, this section examines how DL techniques for super-resolution are making a difference. The introduction emphasized the need for better image detail to support accurate diagnoses and create high-resolution images from lower-quality scans. Related investigations explored how various NN structures are established and how the training datasets, including paired and unpaired ones. Approaches using DL models are beneficial to mitigate the gap between LF and HF imaging quality, enhancing the usefulness of LF-MRI in various clinical situations.

3.1 | Supervised Super-Resolutions: CNN-Based and Residual Learning Architecture

The published studies provided examples of CNN-based implementation on resolution promotion. One of the typical model, U-net, helps in recovering fine details that are often lost during the down-sampling process. The typical symmetric encoder-decoder structure effectively learns to translate low-resolution images into high-resolution sections.

Juan Eugenio Iglesias et al. developed the LF-SynthSR [36] that enhances LF-MRI scans by correlating brain morphometry measurements between the synthetic low field and ground truth high field images. A two-step 3D U-net structure was built that formed a chained network. The first one utilized the previous study SynthSR [92] for super-resolution and the second step was for segmentation. The LF-SynthSR method utilizes a synthetic data generator to expose the CNN to varied images. L1-norm loss and a semantic segmentation loss were used in the first and second U-net steps, respectively. Training data were collected from 20 participants from the OASIS database [93]. LF scans were acquired using the 64mT Hyperfine Swoop MRI system, and the corresponded reference HF data were acquired from 1.5T to 3T [92, 94]. The training dataset, featuring isotropic magnetization-prepared rapid gradient-echo scans, included segmentations of 39 regions of interest (ROIs). During testing, LF scans are co-registered and processed to generate synthetic outputs, which are then segmented with SynthSeg [94, 95]. Following the successful experiments, the poststep experiments, WMH-SynthSeg [96], extended the training dataset to those involving white matter hyperintensities (WMH). The WM-oriented training model automatically calculates ROI volumes on LF images with comparable accuracy to HF-MRI. WMH-SynthSeg enhances robustness by utilizing multitask learning to perform the following three tasks at once: image segmentation, joint synthesis and super-resolution. Unlike SynthSeg, which focuses solely on segmentation, WMH-SynthSeg's multitask U-net predicts all three folds, although it retains only the segmentation outcome during testing.

Another 3D U-net model were investigated by Levente Baljer et al. [18], which achieved the neurodevelopment in infants from South Africa and Malawi, over the first 3 years of life. The well-trained network delivered the clear segmentation of deep brain structures using SynthSeg [95]. Fifty-six subjects ultimately contributing paired LF (Hyperfine 64mT) and HF (Siemens 3T). To explored model performance with varying input scan orientations, the network created three-channel-input, which consists of the following three orthogonal orientations: axial, sagittal, and coronal. Preprocessing techniques include dense-rigid registration and brain extraction via HD-BET. PSNR was selected as loss function to minimize the network parameters. Evaluation used metrics like Dice overlap and tissue volume correlations. Jo Schlemper et al. developed the U-net structure into an unrolling structure with compress sensing [53], that is, a 2D Nonuniform Variational Network (NVN). The NVN architecture consists of multiple learnable blocks, each including a CNN component inspired by U-net for image de-aliasing, a data consistency layer for handling non-uniform *k*-space data, and parameters to balance de-aliasing with data fidelity. Figure 7 directly illustrated the network architecture. The training dataset consisted of 160 ground truth T1 and T2 volumes from the HCP. For evaluation, FLAIR and T2W images from 10 patients were acquired from the Hyperfine POC MRI system (64mT). NVN was compared to other U-net–based methods via metrics as MSE, SSIM, and PSNR. NVN architecture contributes the image reconstruction from under-sampled data and the correction of hardware-induced system imperfections (e.g., encoding errors and eddy currents) in a single, fast (0.3 s/volume) step. Another study concerning fetal MRI was investigated by Kelly Payette et al. [97] involves T2* maps acquired at 0.55T (Siemens' MAGNETOM Free.Max). Segmentation (including lungs, thymus, kidney pelvis, and liver) utilized an existing in-house U-Net using the MONAI

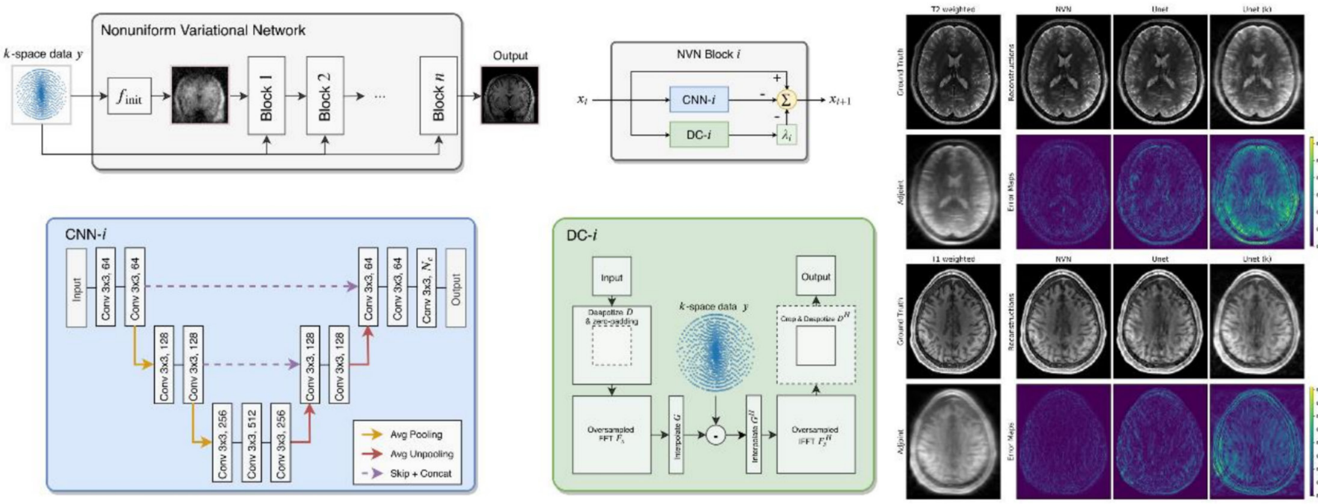

FIGURE 7 | The architecture of Nonuniform Variational Network [53]. Each block has three components: CNN, DC and λ. In detail, DC is a non-Cartesian DC layer and λ is the weighting term. The model has 5 blocks in total. Reconstructions for the T1-weighted (bottom half) and T2-weighted images (top half) from the simulated data acquisition with Hyperfine POC MRI system (64mT, FOV 180 mm × 180 mm × 180 mm, resolution 1.5 mm × 1.5 mm × 5 mm, and the acceleration factor of 3.5).

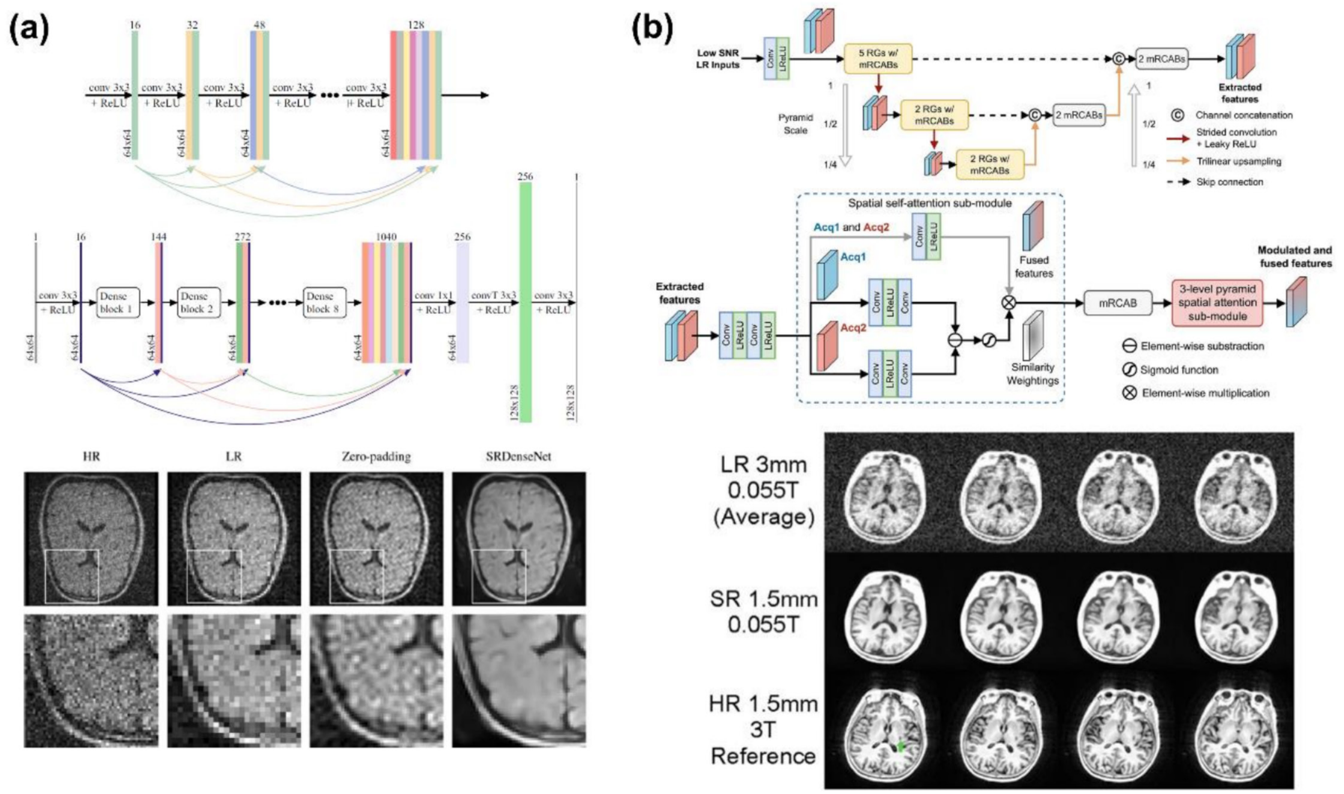

FIGURE 8 | (a) The architecture of SRDenseNet [101], with 8 dense blocks of eight convolutional layers each. Data acquisition was achieved from a home-made 50mT scanner (parameters: FOV 180 mm × 240 mm × 180 mm, 1.5 mm × 1.5 mm × 3 mm, TR/TE = 400 ms/20 ms, echo train length 5, acquisition bandwidth 20 kHz). Results compared a conventional Zero-padding method. (b) Feature extractor module and attention fusion module based on residual channel attention blocks (RCABs) in Vick Lau et al. [106]. SR experiments on the low-resolution home-built 0.055T MRI brain acquired from a 58-year-old female with a small lacunar infarct in the left putamen due to chronic (> 11 months) ischemic stroke (3D T1W, 3-mm^3 resolution, FOVs of 240 mm × 240 mm × 210 mm, acquired via 3D inversion FSE sequence, TR/TE/TI = 590/14/190 ms).

framework [98] with cross-entropy and Dice loss functions, refined by fetal anatomy specialists. However, limitations in this study revealed the lack of standard automated image processing tools, hindering wider clinical use.

In addition to directly training for resolution improvement, Reina Ayde et al. [55] trained a 3D residual U-net model and achieved the acceleration using complex images (both magnitude and phase information). LF datasets were acquired using a custom-built transmit/receive coil at 0.1T MRI [99, 100]. The training dataset involved 10 fully sampled 3D spoiled gradient echo (GRE) scans of the human hand and wrist and underwent preprocessing and data augmentation. L2-norm (MSE) was employed as the loss function. The evaluation involved retrospective analysis using Gaussian sampling patterns to assess performance with a maximum of a fivefold acceleration rate. Validation data consisted of multiple undersampled *k*-space acquisitions to ensure effective reconstruction and performance evaluation against high-field MRI labels.

Despite of U-net–based models, other supervised models also contribute to the super-resolution in LF-MRI. DenseNet was also utilized to train the super-resolution by M. L. de Leeuw den Bouter et al. [101] with the structure consisting of blocks of densely connected convolutional layers [102]. The network is trained on 2D brain images sourced from the NYU fastMRI Initiative database [103, 104], which contains T1, T2, and FLAIR images acquired at 1.5T and 3T. The training used MSE as criteria, and the well-trained network was tested on LF in vivo human brains acquired from a 50mT scanner [105] The network structure is demonstrated in Figure 8a. The network demonstrated a promoted pair-training mode with noise LR and noise-free HF data would recovery anatomical detail while shorten scan times. Vick Lau et al. [106] present a dual-acquisition 3D model, which includes three main components: feature extractor with multiscale residual channel attention blocks (RCABs) [107], attentional fusion module [108], and reconstruction model, trained with L1 loss. A general visualization is witnessed in Figure 8b. Two consecutively acquired 3D MRI datasets were utilized to achieve a 2× up-sampling factor across all spatial dimensions. HF data were derived from the Wu-Minn HCP datasets [109] then down-sampled as training inputs. Evaluation brain data, involving 30 healthy volunteers and 8 patients, were acquired at a home-built 0.055T shield-free scanner [110] and GE 3T Sigma Premier (HF reference). The well-trained network delivered high generalizability from young (e.g., 27 and 33 years male) healthy volunteers to elder patients with brain lesions (e.g., 58-years-old female with small lacunar infarct). Christopher Man [23] applied RCABs structure in the extension study, where the training was built on the down-sampled training data from *k*-space truncations. The proposed Partial super-resolution model (PF-SR) model accelerates the scan time by half in both healthy and pathological brain subjects. PF-SR and Deep-DSP [71] contributed the whole body imaging [22] for speed and quality, testing the 0.055T whole-body MRI scanner on the various body parts: brain, spine (cervical and lumbar), abdomen, lungs, musculoskeletal structures, and the heart (cardiac cine images). Neck angiography was also performed. The two learning-based models were effective in EMI elimination, acceleration, and super-resolution.

3.2 | Self-Supervised Super-Resolution: GAN Model Implementation

An extension study incorporating fundamental CNN structure (e.g., ResNet block) into GAN architecture is published by Sonia Laguna et al. [111]. The key innovation of the training exhibited on the combination of supervised pretraining on high-field data with unsupervised domain adaptation on unpaired scans. The model is established by a Cycle-GAN–based structure, consisting of three modules: domain adaptation (DA), a denoiser, and a super-resolution (SR) module, shown in Figure 9. The DA module combined CycleGAN and FastCUT [112] for unpaired translations, while the SR module utilizes a 3D ESRGAN [113] with 23 residual dense blocks. The training datasets include HF T1/T2 scans from 898 subjects from the HCP and LF Hyperfine scans of 11 subjects from MGH. The SR block was trained with L1 and adversarial losses, the denoiser used L1 loss, and the DA module balanced adversarial and cycle consistency losses. Evaluation was processed thorough the tissue segmentation by SynthSeg [94].

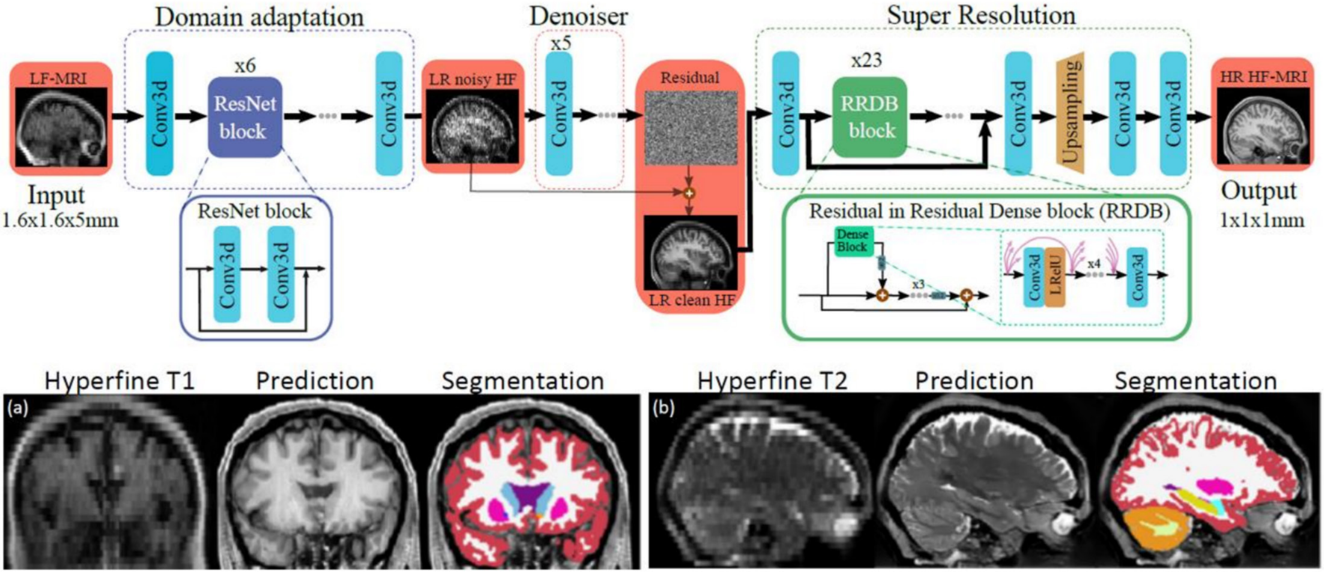

FIGURE 9 | Proposed 3D meta-architecture with building blocks [111]. Experiments were conducted from the Hyperfine 64mT system, resolution 1.5 mm × 1.5 mm × 5 mm. Reconstruction results include sample outputs with FastCUT as DA.

4 | Discussion

This review paper has explored the advancements and challenges in DL-based LF-MRI, highlighting the potential these technologies have for enhancing image quality and diagnostic accuracy. We discussed the motivations for implementing learning-based methods, the importance of data preparation, model architecture, and postprocessing techniques. Furthermore, we addressed the generalization capabilities of trained networks across different datasets. Implementing learning-based methods in LF-MRI is essential because of the need for better imaging in environments with low SNRs [114] and limited spatial resolution. DL techniques offer powerful solutions to these challenges by using neural networks to enhance image quality through advanced filtering and denoising. These methods can learn complex patterns from data, making them particularly suitable for LF-MRI, where traditional methods often fall short in delivering the required accuracy. For clear and comprehensive overview, two comprehensive summary tables were made in Supplementary Tables 1 and 2 to visually synthesize the literature for each study mentioned in Sections 2 and 3.

For conventional end-to-end training, data preparation is a critical factor influencing the final performance of LF learning models [115]. High-quality, well-annotated training datasets are vital for the models to learn meaningful representations of LF-MRI images. Effective data handling, including normalization and noise reduction, enhances the training experience, leading to faster convergence and better performance. Additionally, the use of data augmentation can further improve model robustness by artificially expanding the dataset and capturing a wider range of scenarios. The architecture of the training model also significantly impacts training outcomes. Choosing the right architecture, such as U-Net or other convolutional neural networks, can enhance both accuracy and efficiency. Analyzing various studies reveals insights into effective architectures that provide the best trade-off between complexity and performance. This balance is crucial for optimizing the DL models for LF-MRI, ensuring that they deliver high-quality images without excessive computational demands.

Generalization is another important topic in LF-MRI. Advances in training DL models can lead to systems that perform effectively across multiple datasets. For example, whole-body MRI at 0.05 Tesla [22] demonstrates how a single trained network can yield consistent and reliable results, thus broadening the clinical applicability of LF-MRI. This adaptability suggests that DL models could become vital tools in everyday clinical practice, providing robust solutions to various imaging challenges.

Several promising directions are helpful to training efficiency. The application of unsupervised structures, such as GANs and DMs, offers potential for greater flexibility and efficiency. Techniques like conditional GANs and Cycle-GANs can improve training outcomes by bridging the gap between LF-HF MRI images without needing extensive paired datasets. Additionally, incorporating DMs may enhance the quality of LF-MR images, enabling better representation of anatomical structures. Transfer learning approaches could further streamline the adaptation of models to new datasets, improving their applicability in diverse clinical situations.

Despite the many advancements, there are still limitations and challenges to address. One significant drawback in most DL-based studies is the reliance on large, high-quality annotated datasets, especially on the end-to-end training models. The performance of DL models depends heavily on the quality and diversity of training data. In many cases, obtaining sufficient annotated data can be challenging, particularly for rare conditions in Africa. There are also concerns about the interpretability of DL models; understanding how these models arrive at their decisions is crucial for justifying clinical practices based on their outputs. Explainable AI (XAI) is critical for training interpretability; it bridges the gap between the “black box” learning models and the nonnegotiable need for safety, trust, and clinical accountability in medical diagnosis. XAI techniques, for example, model-specific methods such as LRP [116], illustrate the exact sections of an MRI scan a DL model relied on for its decision. Another category, model-agnostic methods such as LIME [117], explains predictions by approximating the complex model locally with a simpler interpretable one. For conventional HF-MRI implementations, Grad-CAM classifies key regions for brain tumor or Alzheimer's diagnosis from CNNs [118–121]. CAM-based techniques adapted for graph networks pinpoint brain areas associated with conditions like autism [122, 123]. The core result is a saliency map overlaying the scan to show the model's focal regions for its prediction. Successed in HF-MRI applications, these XAI techniques could be further explored to enhance the interpretability and clinical trust in AI models developed for low-field MRI systems.

Moreover, several clinical applications of LF-MRI technology are particularly promising, especially in real-world scenarios involving metallic implants [124–128]. Imaging challenges posed by artifacts from metallic objects often limit traditional MRI techniques. However, advancements in DL-based segmentation and reconstruction have the potential to overcome these barriers, leading to clearer images and more accurate diagnoses. This capability may broaden the use of low-field MRI in institutions with limited access to high-field systems. For future studies, postprocessing algorithms [129–132] for the validation or inference data could be considered as a vital role in refining the images. After initial image reconstruction, techniques such as denoising and artifact correction can enhance image quality further. These refinements are essential for ensuring that images meet the standards required for reliable diagnostic use. Applying robust postprocessing techniques helps mitigate residual noise and improves the overall integrity of the images.

In conclusion, this review highlights the considerable progress made in integrating DL techniques into low-field MRI, solving the key issues as denoising and super-resolution. By emphasizing the importance of data preparation, model selection, and postprocessing, this review demonstrates how these advances can significantly improve imaging outcomes. As the field continues to evolve, ongoing research should address current limitations and explore new model architectures to enhance clinical applications. The potential for low-field MRI to provide valuable diagnostic insights in diverse medical contexts remains significant, contributing to improved patient care and broader access to advanced imaging technologies.

Acknowledgements

We gratefully acknowledge the financial support provided by the National Major Scientific Instruments and Equipments Development Project of National Natural Science Foundation of China (grant number 82527802), the Strategic Priority Research Program of the Chinese Academy of Sciences (grant number XDB1610000) and Hubei Science and Technology Innovation Talent Program (grant number 2024DJA001). Figures reproduced in this review article have been granted permissions from authors and/or publishers. Payments are made when necessary:

Figures 1, 2c, and 8b: Reproduced with permission from Ed X. Wu et al., Deep Learning Enabled Fast 3D brain MRI at 0.055 Tesla (Science Advances, 2023); Robust EMI Elimination for RF Shielding-Free MRI Through Deep Learning Direct MR Signal Prediction (Magnetic Resonance in Medicine, 2023); Pushing the Limits of Low-Cost Ultra-Low-Field MRI by Dual-Acquisition Deep Learning 3D Superresolution (Magnetic Resonance in Medicine, 2022).

Figure 2a: Reproduced with permission from Springer, Deep Learning for Low-Field to High-Field MR: Image Quality Transfer With Probabilistic Decimation Simulator (MLMIR 2019).

Figures 2b, 3c, 4a, 4b, and 6b: Reproduced with permission from the ITEE Permissions Team, Improving image quality in low-field MRI with deep learning (ICIP, 2021); Ultra Low-Field to High-Field MRI Translation Using Adversarial Diffusion (ISBI, 2024); Ultra-Low Field Magnetic Resonance Image Enhancement based on Deep-Learning Method (ICHIH 2023); Deep-Learning-Based Dual Denoising Algorithm for Shielding-Free Magnetic Resonance Imaging (IEEE Transactions on Artificial Intelligence, 2025); Electromagnetic Interference Rejection Strategy for 50 mT Portable Unshielded Whole-body Magnetic Resonance Imaging with A Convolutional Neural Network Incorporating Attention Mechanism (IEEE Transactions on Instrumentation and Measurement, 2025).

Figure 3a: Reproduced with permission from Matthew Rosen et al., Boosting the signal-to-noise of low-field MRI with deep learning image reconstruction, (Scientific Reports, 2021).

Figure 3b: Reproduced with permission from Elsevier, ArtifactID: Identifying Artifacts in Low-Field MRI of the Brain Using Deep Learning (Magnetic Resonance Imaging, 2022).

Figure 5: Reproduced with permission from Fernando Vega et al., Denoising Simulated Low-Field MRI (70mT) using DAE and Cycle-GAN (arXiv:2307.06338, 2023).

Figure 6a: Reproduced with permission from Hongjiang Wei et al., Zero-Shot Low-Field MRI Enhancement via Denoising Diffusion Driven Neural Representation, MICCAI 2024.

Figure 7: Reproduced with permission from ISMRM Permissions Team, Deep Learning MRI Reconstruction in Application to Point-of-Care MRI (ISMRM 2020).

Figure 8a: Reproduced with permission from Merel de Leeuw den Bouter et al., Deep Learning-Based Single Image Super-Resolution for Low-Field MR Brain Images (Scientific Reports, 2022).

Figure 9: Reproduced with permission from Juan Eugenio Iglesias et al., Super-Resolution of Portable Low-Field MRI in Real Scenarios: Integration With Denoising and Domain Adaptation (Medical Imaging with Deep Learning, 2022).

Data Availability Statement

Data sharing not applicable to this article as no datasets were generated or analysed during the current study.

References

1. M. T. Vlaardingerbroek and J. A. Boer, *Magnetic Resonance Imaging: Theory and Practice* (Springer Science & Business Media, 2013).

2. V. Muñoz-Ramírez, V. Kmetzsch, F. Forbes, S. Meoni, E. Moro, and M. Dojat, "Subtle Anomaly Detection: Application to Brain MRI Analysis of De Novo Parkinsonian Patients," *Artificial Intelligence in Medicine* 125 (2022): 102251.

3. V. R. Fuchs and H. C. Sox, Jr., "Physicians' Views of the Relative Importance of Thirty Medical Innovations," *Health Aff (Millwood)* 20, no. 5 (2001): 30–42.

4. M. Hori, A. Hagiwara, M. Goto, A. Wada, and S. Aoki, "Low-Field Magnetic Resonance Imaging: Its History and Renaissance," *Investigative Radiology* 56, no. 11 (2021): 669–679.

5. W. T. Kimberly, A. J. Sorby-Adams, A. G. Webb, et al., "Brain Imaging With Portable Low-Field MRI," *Nature Reviews Bioengineering* 1, no. 9 (2023): 617–630.

6. J. P. Marques, F. F. Simonis, and A. G. Webb, "Low-Field MRI: An MR Physics Perspective," *Journal of Magnetic Resonance Imaging* 49, no. 6 (2019): 1528–1542.

7. M. Sarracanie and N. Salameh, "Low-Field MRI: How Low Can We Go? A Fresh View on an Old Debate," *Frontiers in Physics* 8 (2020): 172.

8. J. Vosshenrich, H.-C. Breit, M. Bach, and E. M. Merkle, "Economic Aspects of Low-Field Magnetic Resonance Imaging: Acquisition, Installation, and Maintenance Costs of 0.55 T Systems," *Der Radiologe* 62, no. 5 (2022): 400–404.

9. A. E. Campbell-Washburn, K. E. Keenan, P. Hu, et al., "Low-Field MRI: A Report on the 2022 ISMRM Workshop," *Magnetic Resonance in Medicine* 90, no. 4 (2023): 1682–1694.

10. S. S. Bhat, T. T. Fernandes, P. Poojar, et al., "Low-Field MRI of Stroke: Challenges and Opportunities," *Journal of Magnetic Resonance Imaging* 54, no. 2 (2021): 372–390.

11. W. Bian, "A Review of Electromagnetic Elimination Methods for Low-Field Portable MRI Scanner," arXiv preprint arXiv:240617804 (2024).

12. F. Hasford, A. N. Mumuni, C. Trauernicht, et al., "A Review of MRI Studies in Africa With Special Focus on Quantitative MRI: Historical Development, Current Status and the Role of Medical Physicists," *Physica Medica* 103 (2022): 46–58.

13. G. I. Ogbole, A. O. Adeyomoye, A. Badu-Peprah, Y. Mensah, and D. A. Nzeh, "Survey of Magnetic Resonance Imaging Availability in West Africa," *Pan African Medical Journal* 30, no. 1 (2018): 240.

14. H. Qu, H. Wang, Q. Chen, C. Wang, X. Liu, and Q. Wang, "An Experimental Study on the Passive Shimming in the 0.5 T Superconducting MRI Magnet," *IEEE Transactions on Applied Superconductivity* 32, no. 7 (2022): 1–7.

15. V. M. Runge and J. T. Heverhagen, "Advocating the Development of Next-Generation, Advanced-Design Low-Field Magnetic Resonance Systems," *Investigative Radiology* 55, no. 12 (2020): 747–753.

16. T. Rusche, J. Vosshenrich, D. J. Winkel, et al., "More Space, Less Noise—New-Generation Low-Field Magnetic Resonance Imaging Systems Can Improve Patient Comfort: A Prospective 0.55 T–1.5 T-Scanner Comparison," *Journal of Clinical Medicine* 11, no. 22 (2022): 6705.

17. G. Lemberskiy, H. Chandarana, M. Bruno, et al., "Feasibility of Accelerated Prostate Diffusion-Weighted Imaging on 0.55 T MRI Enabled With Random Matrix Theory Denoising," *Investigative Radiology* 58, no. 10 (2023): 720–729.

18. L. Baljer, Y. Zhang, N. Bourke, et al., "Multi-Orientation U-Net for Super-Resolution of Ultra-Low-Field Paediatric MRI," (2024).

19. K. T. Islam, S. Zhong, P. Zakavi, et al., “Improving Portable Low-Field MRI Image Quality Through Image-to-Image Translation Using Paired Low- and High-Field Images,” *Scientific Reports* 13, no. 1 (2023): 21183.

20. K. V. Jordanova, M. N. Martin, S. E. Ogier, M. E. Poorman, and K. E. Keenan, “In Vivo Quantitative MRI: T 1 and T 2 Measurements of the Human Brain at 0.064 T,” *Magnetic Resonance Materials in Physics, Biology and Medicine* 36, no. 3 (2023): 487–498.

21. F. Meng, Y. Guo, W. He, and Z. Xu, eds., “Ultra-Low Field Magnetic Resonance Image Enhancement Based on Deep-Learning Method,” in *2023 2nd International Conference on Health Big Data and Intelligent Healthcare (ICHIH)* (IEEE, 2023).

22. Y. Zhao, Y. Ding, V. Lau, et al., “Whole-Body Magnetic Resonance Imaging at 0.05 Tesla,” *Science* 384, no. 6696 (2024): eadm7168.

23. C. Man, V. Lau, S. Su, et al., “Deep Learning Enabled Fast 3D Brain MRI at 0.055 Tesla,” *Science Advances* 9, no. 38 (2023): eadi9327.

24. S. C. Deoni, M. M. Bruchhage, J. Beauchemin, et al., “Accessible Pediatric Neuroimaging Using a Low Field Strength MRI Scanner,” *NeuroImage* 238 (2021): 118273.

25. T. C. Arnold, C. W. Freeman, B. Litt, and J. M. Stein, “Low-Field MRI: Clinical Promise and Challenges,” *Journal of Magnetic Resonance Imaging* 57, no. 1 (2023): 25–44.

26. A. S. Shetty, D. R. Ludwig, J. E. Ippolito, T. J. Andrews, V. R. Narra, and T. J. Fraum, “Low-Field-Strength Body MRI: Challenges and Opportunities at 0.55 T,” *Radiographics* 43, no. 12 (2023): e230073.

27. F. Resmer, H. C. Seton, and J. M. Hutchison, “Cryogenic Receive Coil and Low Noise Preamplifier for MRI at 0.01 T,” *Journal of Magnetic Resonance* 203, no. 1 (2010): 57–65.

28. J. A. Nordmeyer-Massner, N. De Zanche, and K. P. Pruessmann, “Noise Figure Characterization of Preamplifiers at NMR Frequencies,” *Journal of Magnetic Resonance* 210, no. 1 (2011): 7–15.

29. T. Yamashita, T. Oida, S. Hamada, and T. Kobayashi, “Thermal Noise Calculation Method for Precise Estimation of the Signal-To-Noise Ratio of Ultra-Low-Field MRI With an Atomic Magnetometer,” *Journal of Magnetic Resonance* 215 (2012): 100–108.

30. J. Bodurka, F. Ye, N. Petridou, K. Murphy, and P. A. Bandettini, “Mapping the MRI Voxel Volume in Which Thermal Noise Matches Physiological Noise—Implications for fMRI,” *NeuroImage* 34, no. 2 (2007): 542–549.

31. L. Vizioli, S. Moeller, L. Dowdle, et al., “Lowering the Thermal Noise Barrier in Functional Brain Mapping With Magnetic Resonance Imaging,” *Nature Communications* 12, no. 1 (2021): 5181.

32. J. Parsa, T. O'Reilly, and A. Webb, “A Single-Coil-Based Method for Electromagnetic Interference Reduction in Point-of-Care Low Field MRI Systems,” *Journal of Magnetic Resonance* 346 (2023): 107355.

33. M. Yu, Q. Tao, H. Dong, et al., “Ultra-Low Noise Graphene/Copper/Nylon Fabric for Electromagnetic Interference Shielding in Ultra-Low Field Magnetic Resonance Imaging,” *Journal of Magnetic Resonance* 317 (2020): 106775.

34. S. A. Srinivas, S. F. Cauley, J. P. Stockmann, et al., “External Dynamic Interference Estimation and Removal (EDITER) for Low Field MRI,” *Magnetic Resonance in Medicine* 87, no. 2 (2022): 614–628.

35. C. Liu, B. Chang, L. Qiu, et al., “Effect of Magnetic Field Fluctuation on Ultra-Low Field MRI Measurements in the Unshielded Laboratory Environment,” *Journal of Magnetic Resonance* 257 (2015): 8–14.

36. J. E. Iglesias, R. Schleicher, S. Laguna, et al., “Quantitative Brain Morphometry of Portable Low-Field-Strength MRI Using Super-Resolution Machine Learning,” *Radiology* 306, no. 3 (2022): e220522.

37. C. Donnay, S. V. Okar, C. Tsagkas, et al., “Super Resolution Using Sparse Sampling at Portable Ultra-Low Field MR,” *Frontiers in Neurology* 15 (2024): 1330203.

38. A. P. Mahmoudzadeh and N. H. Kashou, “Interpolation-Based Super-Resolution Reconstruction: Effects of Slice Thickness,” *Journal of Medical Imaging* 1, no. 3 (2014): 034007.

39. Y. C. Hsu, P. T. Vesanen, J. O. Nieminen, et al., “Efficient Concomitant and Remanence Field Artifact Reduction in Ultra-Low-Field MRI Using a Frequency-Space Formulation,” *Magnetic Resonance in Medicine* 71, no. 3 (2014): 955–965.

40. Y. Zhang, W. He, F. Chen, J. Wu, Y. He, and Z. Xu, “Denoise Ultra-Low-Field 3D Magnetic Resonance Images Using a Joint Signal-Image Domain Filter,” *Journal of Magnetic Resonance* 344 (2022): 107319.

41. O. Ronneberger, P. Fischer, and T. Brox, eds., “U-net: Convolutional Networks for Biomedical Image Segmentation,” in *Medical Image Computing and Computer-Assisted Intervention–MICCAI 2015: 18th International Conference, Munich, Germany, October 5–9, 2015, Proceedings, Part III 18* (Springer, 2015).

42. J. Long, E. Shelhamer, and T. Darrell, eds., “Fully Convolutional Networks for Semantic Segmentation,” in *Proceedings of the IEEE Conference on Computer Vision and Pattern Recognition* (IEEE, 2015).

43. L. Xu, J. S. Ren, C. Liu, and J. Jia, “Deep Convolutional Neural Network for Image Deconvolution,” Advances in Neural Information Processing Systems. (2014): 27.

44. I. Goodfellow, J. Pouget-Abadie, M. Mirza, et al., “Generative Adversarial Nets,” *Advances in Neural Information Processing Systems* (2014): 27.

45. J. Gauthier, “Conditional Generative Adversarial Nets for Convolutional Face Generation,” Class Project for Stanford CS231N: Convolutional Neural Networks for Visual Recognition, Winter Semester 2014 (5) (2014): 2.

46. M. Mirza, “Conditional Generative Adversarial Nets,” arXiv preprint arXiv:1411.1784 (2014).

47. J. Y. Zhu, T. Park, P. Isola, A. A. Efros, Ed. “Unpaired Image-to-Image Translation Using Cycle-Consistent Adversarial Networks,” Proceedings of the IEEE International Conference on Computer Vision (2017).

48. D. Yoo, Y. A. Choi, C. Rah, et al., “Signal Enhancement of Low Magnetic Field Magnetic Resonance Image Using a Conventional- and Cyclic-Generative Adversarial Network Models With Unpaired Image Sets,” *Frontiers in Oncology* 11 (2021): 660284.

49. F. Vega, A. Addeh, and M. E. MacDonald, “Denoising Simulated Low-Field MRI (70mT) Using Denoising Autoencoders (DAE) and Cycle-Consistent Generative Adversarial Networks (Cycle-GAN),” arXiv preprint arXiv:230706338 (2023).

50. J. Ho, A. Jain, and P. Abbeel, “Denoising Diffusion Probabilistic Models,” *Advances in Neural Information Processing Systems* 33 (2020): 6840–6851.

51. Z. Zhu, A. Rehman, X. Cao, et al., “Advancing Low-Field MRI With a Universal Denoising Imaging Transformer: Towards Fast and High-Quality Imaging,” arXiv preprint arXiv:240419167 (2024).

52. B. Zhou, J. Schlemper, N. Dey, et al., “Dual-Domain Self-Supervised Learning for Accelerated Non-Cartesian MRI Reconstruction,” *Medical Image Analysis* 81 (2022): 102538.

53. J. Schlemper, S. S. M. Salehi, C. Lazarus, et al., Ed., “Deep Learning MRI Reconstruction in Application to Point-Of-Care MRI,” Proc Intl Soc Mag Reson Med (2020).

54. B. Zhu, J. Z. Liu, S. F. Cauley, B. R. Rosen, and M. S. Rosen, “Image Reconstruction by Domain-Transform Manifold Learning,” *Nature* 555, no. 7697 (2018): 487–492.

55. R. Ayde, T. Senft, N. Salameh, and M. Sarracanie, "Deep Learning for Fast Low-Field MRI Acquisitions," *Scientific Reports* 12, no. 1 (2022): 11394.

56. E. Ahishakiye, M. B. Van Gijzen, J. Tumwiine, and J. Obungoloch, "Adaptive-Size Dictionary Learning Using Information Theoretic Criteria for Image Reconstruction From Undersampled K-Space Data in Low Field Magnetic Resonance Imaging," *BMC Medical Imaging* 20, no. 1 (2020): 72.

57. S. Ravishankar and Y. Bresler, "MR Image Reconstruction From Highly Undersampled K-Space Data by Dictionary Learning," *IEEE Transactions on Medical Imaging* 30, no. 5 (2010): 1028–1041.

58. W. Bian, P. Li, M. Zheng, et al., eds., "A Review of Electromagnetic Elimination Methods for Low-Field Portable MRI Scanner," in *2024 5th International Conference on Machine Learning and Computer Application (ICMLCA)* (IEEE, 2024).

59. C. Zegers, J. Posch, A. Traverso, et al., "Current Applications of Deep-Learning in Neuro-Oncological MRI," *Physica Medica* 83 (2021): 161–173.

60. J. E. Park, H. S. Kim, D. Kim, et al., "A Systematic Review Reporting Quality of Radiomics Research in Neuro-Oncology: Toward Clinical Utility and Quality Improvement Using High-Dimensional Imaging Features," *BMC Cancer* 20, no. 1 (2020): 29.

61. S. Chauvie, L. N. Mazzoni, and J. O'Doherty, "A Review on the Use of Imaging Biomarkers in Oncology Clinical Trials: Quality Assurance Strategies for Technical Validation," *Tomography* 9, no. 5 (2023): 1876–1902.

62. L. Pasquini, K. K. Peck, M. Jenabi, and A. Holodny, "Functional MRI in Neuro-Oncology: State of the Art and Future Directions," *Radiology* 308, no. 3 (2023): e222028.

63. M. M. Shaver, P. A. Kohanteb, C. Chiou, et al., "Optimizing Neuro-Oncology Imaging: A Review of Deep Learning Approaches for Glioma Imaging," *Cancers* 11, no. 6 (2019): 829.

64. A. Aghabiglou and E. M. Eksioglu, "Projection-Based Cascaded U-Net Model for MR Image Reconstruction," *Computer Methods and Programs in Biomedicine* 207 (2021): 106151.

65. D. Mehta, D. Padalia, K. Vora, and N. Mehendale, eds., "MRI image Denoising Using U-Net and Image Processing Techniques," in *2022 5th International Conference on Advances in Science and Technology (ICAST)* (IEEE, 2022).

66. J. V. Manjón and P. Coupe, eds., "MRI Denoising Using Deep Learning," in *Patch-Based Techniques in Medical Imaging: 4th International Workshop, Patch-MI 2018, Held in Conjunction With MICCAI 2018, Granada, Spain, September 20, 2018, Proceedings 4* (Springer, 2018).

67. L. Zhang, M. Wu, L. Wang, D. C. Steffens, G. G. Potter, and M. Liu, "Iterative Learning for Joint Image Denoising and Motion Artifact Correction of 3D Brain MRI," arXiv preprint arXiv:240308162 (2024).

68. P. L. K. Ding, Z. Li, Y. Zhou, and B. Li, eds., "Deep Residual Dense U-Net for Resolution Enhancement in Accelerated MRI Acquisition," in *Medical Imaging 2019: Image Processing* (SPIE, 2019).

69. H. Lin, M. Figini, R. Tanno, et al., eds., "Deep Learning for Low-Field to High-Field MR: Image Quality Transfer With Probabilistic Decimation Simulator," in *Machine Learning for Medical Image Reconstruction: Second International Workshop, MLMIR 2019, Held in Conjunction With MICCAI 2019, Shenzhen, China, October 17, 2019, Proceedings 2* (Springer, 2019).

70. A. G. Hernandez, P. Fau, S. Rapacchi, et al., eds., "Improving Image Quality in Low-Field MRI With Deep Learning," in *2021 IEEE International Conference on Image Processing (ICIP)* (IEEE, 2021).

71. Y. Zhao, L. Xiao, J. Hu, and E. X. Wu, "Robust EMI Elimination for RF Shielding-Free MRI Through Deep Learning Direct MR Signal Prediction," *Magnetic Resonance in Medicine* 92, no. 1 (2024): 112–127.

72. C. Dong, C. C. Loy, and X. Tang, eds., "Accelerating the Super-Resolution Convolutional Neural Network," in *Computer Vision–ECCV 2016: 14th European Conference, Amsterdam, The Netherlands, October 11–14, 2016, Proceedings, Part II 14* (Springer, 2016).

73. K. He, X. Zhang, S. Ren, and J. Sun, Ed., "Deep Residual Learning for Image Recognition. Proceedings of the IEEE Conference on Computer Vision and Pattern Recognition," (2016).

74. M. E. MacDonald, E. Fikre, F. Vega, and A. Addeh, Ed., "Simulation Evidence for Use of a Denoising Auto-Encoder (DAE) to Improve Ultra-Low Field (64mt) MRI With a High Field (3T) Prior 2022: ISMRM,".

75. B. Lorch, G. Vaillant, C. Baumgartner, W. Bai, D. Rueckert, and A. Maier, "Automated Detection of Motion Artefacts in MR Imaging Using Decision Forests," *Journal of Medical Engineering* 2017, no. 1 (2017): 4501647.

76. D. Schote, L. Winter, C. Kolbitsch, G. Rose, O. Speck, and A. Kofler, "Joint $\mathrm {{B}} _ {0} $ and Image Reconstruction in Low-Field MRI by Physics-Informed Deep-Learning," *IEEE Transactions on Biomedical Engineering* 71, no. 10 (2024): 2842–2853.

77. N. Koonjoo, B. Zhu, G. C. Bagnall, D. Bhutto, and M. Rosen, "Boosting the Signal-to-Noise of Low-Field MRI With Deep Learning Image Reconstruction," *Scientific Reports* 11, no. 1 (2021): 8248.

78. M. M. Jimeno, K. S. Ravi, Z. Jin, D. Oyekunle, G. Ogbole, and S. Geethanath, "ArtifactID: Identifying Artifacts in Low-Field MRI of the Brain Using Deep Learning," *Magnetic Resonance Imaging* 89 (2022): 42–48.

79. R. R. Selvaraju, M. Cogswell, A. Das, R. Vedantam, D. Parikh, and D. Batra, Ed., "Grad-Cam: Visual Explanations From Deep Networks via Gradient-Based Localization," Proceedings of the IEEE International Conference on Computer Vision (2017).

80. Y. Hu, Y. Huang, S. Qu, Y. Xie, Y. Fang, and X. Zhang, "Deep-Learning-Based Dual Denoising Algorithm for Shielding-Free Magnetic Resonance Imaging," *IEEE Transactions on Artificial Intelligence* 6 (2025): 2766–2776.

81. R. Lu, Z. Wu, G. Zhang, et al., "Electromagnetic Interference Rejection Strategy for 50 mT Portable Unshielded Whole-Body Magnetic Resonance Imaging With a Convolutional Neural Network Incorporating Attention Mechanism," *IEEE Transactions on Instrumentation and Measurement* 74 (2025): 1–8.

82. P. J. LaMontagne, T. L. Benzinger, J. C. Morris, et al., "OASIS-3: Longitudinal Neuroimaging, Clinical, and Cognitive Dataset for Normal Aging and Alzheimer Disease," Medrxiv (2019): 2019.12.13.19014902.

83. F.-A. Croitoru, V. Hondru, R. T. Ionescu, and M. Shah, "Diffusion Models in Vision: A Survey," *IEEE Transactions on Pattern Analysis and Machine Intelligence* 45, no. 9 (2023): 10850–10869.

84. F. Khader, G. Müller-Franzes, S. Tayebi Arasteh, et al., "Denoising Diffusion Probabilistic Models for 3D Medical Image Generation," *Scientific Reports* 13, no. 1 (2023): 7303.

85. Z. Dorjsembe, S. Odonchimed, and F. Xiao, Ed., "Three-Dimensional Medical Image Synthesis With Denoising Diffusion Probabilistic Models," Medical Imaging With Deep Learning (2022).

86. X. Lin, C. Du, Q. Wu, et al., eds., "Zero-Shot Low-Field MRI Enhancement via Denoising Diffusion Driven Neural Representation," in *International Conference on Medical Image Computing and Computer-Assisted Intervention* (Springer, 2024).

87. Y. Song, J. Sohl-Dickstein, D. P. Kingma, A. Kumar, S. Ermon, and B. Poole, "Score-Based Generative Modeling Through Stochastic Differential Equations," arXiv preprint arXiv:201113456. (2020).

88. Q. Wu, Y. Li, Y. Sun, et al., "An Arbitrary Scale Super-Resolution Approach for 3D MR Images via Implicit Neural Representation,"

IEEE Journal of Biomedical and Health Informatics 27, no. 2 (2022): 1004–1015.

89. Q. Wu, Y. Li, L. Xu, et al., "IREM: High-Resolution Magnetic Resonance Image Reconstruction via Implicit Neural Representation," in *Medical Image Computing and Computer Assisted Intervention–MICCAI 2021: 24th International Conference, Strasbourg, France, September 27–October 1, 2021, Proceedings, Part VI*, vol. 24, ed. W. Li, X. Feng, W. Yang, et al. (Springer, 2021).

90. S. Dayarathna, K. T. Islam, and Z. Chen, "Ultra Low-Field to High-Field MRI Translation Using Adversarial Diffusion," in *2024 IEEE International Symposium on Biomedical Imaging (ISBI)* (IEEE, 2024).

91. Z. Xiao, K. Kreis, and A. Vahdat, "Tackling the Generative Learning Trilemma With Denoising Diffusion GANs," arXiv preprint arXiv:2112.07804 (2021).

92. B. Billot, E. Robinson, A. V. Dalca, and J. E. Iglesias, eds., "Partial Volume Segmentation of Brain MRI Scans of Any Resolution and Contrast," in *Medical Image Computing and Computer Assisted Intervention–MICCAI 2020: 23rd International Conference, Lima, Peru, October 4–8, 2020, Proceedings, Part VII 23* (Springer, 2020).

93. D. S. Marcus, T. H. Wang, J. Parker, J. G. Csernansky, J. C. Morris, and R. L. Buckner, "Open Access Series of Imaging Studies (OASIS): Cross-Sectional MRI Data in Young, Middle Aged, Nondemented, and Demented Older Adults," *Journal of Cognitive Neuroscience* 19, no. 9 (2007): 1498–1507.

94. B. Billot, D. Greve, K. Van Leemput, B. Fischl, J. E. Iglesias, and A. V. Dalca, "A Learning Strategy for Contrast-Agnostic MRI Segmentation," arXiv preprint arXiv:200301995 (2020).

95. J. E. Iglesias, B. Billot, Y. Balbastre, et al., "Joint Super-Resolution and Synthesis of 1 mm Isotropic MP-RAGE Volumes From Clinical MRI Exams With Scans of Different Orientation, Resolution and Contrast," *NeuroImage* 237 (2021): 118206.

96. A. J. Sorby-Adams, J. Guo, P. Laso, et al., "Portable, Low-Field Magnetic Resonance Imaging for Evaluation of Alzheimer's Disease," *Nature Communications* 15, no. 1 (2024): 1–12.

97. K. Payette, A. Uus, J. Aviles Verdera, et al., eds., "An automated Pipeline for Quantitative T2* Fetal Body MRI and Segmentation at Low Field," in *International Conference on Medical Image Computing and Computer-Assisted Intervention* (Springer, 2023).

98. MONAI Consortium M, "MONAI: Medical Open Network for AI," https://doi.org/10.5281/zenodo.5525502.

99. M. Sarracanie, "Fast Quantitative Low-Field Magnetic Resonance Imaging With OPTIMUM—Optimized Magnetic Resonance Fingerprinting Using a Stationary Steady-State Cartesian Approach and Accelerated Acquisition Schedules," *Investigative Radiology* 57, no. 4 (2022): 263–271.

100. A. Constantinesco, P. Choquet, G. Cauffet, et al., "Low-Field Dedicated and Desktop Magnetic Resonance Imaging Systems for Agricultural and Food Applications," *Magnetic Resonance in Chemistry* 35, no. 13 (1997): S69–S75.

101. M. de Leeuw Den Bouter, G. Ippolito, T. O'Reilly, R. Remis, M. Van Gijzen, and A. Webb, "Deep Learning-Based Single Image Super-Resolution for Low-Field MR Brain Images," *Scientific Reports* 12, no. 1 (2022): 6362.

102. G. Huang, Z. Liu, Van Der Maaten, L, and Weinberger, KQ, Ed., "Densely Connected Convolutional Networks," Proceedings of the IEEE Conference on Computer Vision and Pattern Recognition (2017).

103. F. Knoll, J. Zbontar, A. Sriram, et al., "FastMRI: A Publicly Available Raw K-Space and DICOM Dataset of Knee Images for Accelerated MR Image Reconstruction Using Machine Learning," *Radiology: Artificial Intelligence* 2, no. 1 (2020): e190007.

104. J. Zbontar, F. Knoll, A. Sriram, et al., "FastMRI: An Open Dataset and Benchmarks for Accelerated MRI," arXiv preprint arXiv:181108839 (2018).

105. T. O'Reilly, W. M. Teeuwisse, D. de Gans, K. Koolstra, and A. G. Webb, "In Vivo 3D Brain and Extremity MRI at 50 mT Using a Permanent Magnet Halbach Array," *Magnetic Resonance in Medicine* 85, no. 1 (2021): 495–505.

106. V. Lau, L. Xiao, Y. Zhao, et al., "Pushing the Limits of Low-Cost Ultra-Low-Field MRI by Dual-Acquisition Deep Learning 3D Superresolution," *Magnetic Resonance in Medicine* 90, no. 2 (2023): 400–416.

107. Y. Zhang, K. Li, K. Li, L. Wang, B. Zhong, and Y. Fu, Ed., "Image Super-Resolution Using Very Deep Residual Channel Attention Networks," Proceedings of the European Conference on Computer Vision (ECCV) (2018).

108. Y. Dai, F. Gieseke, S. Oehmcke, Y. Wu, and K. Barnard, Ed., "Attentional Feature Fusion," Proceedings of the IEEE/CVF Winter Conference on Applications of Computer Vision (2021).

109. D. C. Van Essen, S. M. Smith, D. M. Barch, et al., "The WU-Minn Human Connectome Project: An Overview," *NeuroImage* 80 (2013): 62–79.

110. A. T. Leong, Y. Liu, Y. Zhao, et al., "A Feasibility Study of 0.055 T MRI for Neuroimaging and Comparison With Clinical 3T MRI," Proceedings of the 31st Annual Meeting of ISMRM (2022).

111. S. Laguna, R. Schleicher, B. Billot, et al., Ed., "Super-Resolution of Portable Low-Field MRI in Real Scenarios: Integration With Denoising and Domain Adaptation," Medical Imaging With Deep Learning (2022).

112. T. Park, A. A. Efros, R. Zhang, and J.-Y. Zhu, eds., "Contrastive Learning for Unpaired Image-to-Image Translation," in *Computer Vision–ECCV 2020: 16th European Conference, Glasgow, UK, August 23–28, 2020, Proceedings, Part IX 16* (Springer, 2020).

113. X. Wang, K. Yu, S. Wu, et al., Ed., "Esrgan: Enhanced Super-Resolution Generative Adversarial Networks," Proceedings of the European Conference on Computer Vision (ECCV) Workshops (2018).

114. R. Ayde, M. Vornehm, Y. Zhao, F. Knoll, E. X. Wu, and M. Sarracanie, "MRI at Low Field: A Review of Software Solutions for Improving SNR," *NMR in Biomedicine* 38, no. 1 (2025): e5268.

115. M. Paul, S. Ganguli, and G. K. Dziugaite, "Deep Learning on a Data Diet: Finding Important Examples Early in Training," *Advances in Neural Information Processing Systems* 34 (2021): 20596–20607.

116. S. Bach, A. Binder, G. Montavon, F. Klauschen, K.-R. Müller, and W. Samek, "On Pixel-Wise Explanations for Non-Linear Classifier Decisions by Layer-Wise Relevance Propagation," *PLoS ONE* 10, no. 7 (2015): e0130140.

117. M. T. Ribeiro, S. Singh, and C. Guestrin, Ed., ""Why Should I Trust You?" Explaining the Predictions of Any Classifier," Proceedings of the 22nd ACM SIGKDD International Conference on Knowledge Discovery and Data Mining (2016).

118. M. Böhle, F. Eitel, M. Weygandt, and K. Ritter, "Layer-Wise Relevance Propagation for Explaining Deep Neural Network Decisions in MRI-Based Alzheimer's Disease Classification," *Frontiers in Aging Neuroscience* 11 (2019): 194.

119. R. Ceschin, A. Zahner, W. Reynolds, et al., "A Computational Framework for the Detection of Subcortical Brain Dysmaturation in Neonatal MRI Using 3D Convolutional Neural Networks," *NeuroImage* 178 (2018): 183–197.

120. S. Pereira, R. Meier, V. Alves, M. Reyes, and C. A. Silva, eds., "Automatic Brain Tumor Grading From MRI Data Using Convolutional Neural Networks and Quality Assessment," in *International Workshop on Machine Learning in Clinical Neuroimaging* (Springer, 2018).

121. P. Windisch, P. Weber, C. Fürweger, et al., “Implementation of Model Explainability for a Basic Brain Tumor Detection Using Convolutional Neural Networks on MRI Slices,” *Neuroradiology* 62, no. 11 (2020): 1515–1518.

122. G. Wen, P. Cao, H. Bao, W. Yang, T. Zheng, and O. Zaiane, “MVS-GCN: A Prior Brain Structure Learning-Guided Multi-View Graph Convolution Network for Autism Spectrum Disorder Diagnosis,” *Computers in Biology and Medicine* 142 (2022): 105239.

123. S. Zhang, J. Wang, S. Yu, et al., “An Explainable Deep Learning Framework for Characterizing and Interpreting Human Brain States,” *Medical Image Analysis* 83 (2023): 102665.

124. I. Khodarahmi, I. M. Brinkmann, D. J. Lin, et al., “New-Generation Low-Field Magnetic Resonance Imaging of Hip Arthroplasty Implants Using Slice Encoding for Metal Artifact Correction: First In Vitro Experience at 0.55 T and Comparison With 1.5 T,” *Investigative Radiology* 57, no. 8 (2022): 517–526.

125. A. E. Campbell-Washburn, J. Varghese, K. S. Nayak, R. Ramasawmy, and O. P. Simonetti, “Cardiac MRI at Low Field Strengths,” *Journal of Magnetic Resonance Imaging* 59, no. 2 (2024): 412–430.

126. H.-C. Breit, J. Vosshenrich, M. Clauss, et al., “Visual and Quantitative Assessment of Hip Implant-Related Metal Artifacts at Low Field MRI: A Phantom Study Comparing a 0.55-T System With 1.5-T and 3-T Systems,” *European Radiology Experimental* 7, no. 1 (2023): 5.

127. E. Peschke, P. Ulloa, O. Jansen, and J.-B. Hoevener, eds., “Metallic Implants in MRI–Hazards and Imaging Artifacts,” in *RöFo-Fortschritte auf dem Gebiet der Röntgenstrahlen und der bildgebenden Verfahren* (Georg Thieme Verlag KG, 2021).

128. C. Van Speybroeck, T. O'Reilly, W. Teeuwisse, P. Arnold, and A. Webb, “Characterization of Displacement Forces and Image Artifacts in the Presence of Passive Medical Implants in Low-Field (<100 mT) Permanent Magnet-Based MRI Systems, and Comparisons With Clinical MRI Systems,” *Physica Medica* 84 (2021): 116–124.

129. H. Chang and J. M. Fitzpatrick, “A Technique for Accurate Magnetic Resonance Imaging in the Presence of Field Inhomogeneities,” *IEEE Transactions on Medical Imaging* 11, no. 3 (1992): 319–329.

130. C. A. Michal, “Low-Cost Low-Field NMR and MRI: Instrumentation and Applications,” *Journal of Magnetic Resonance* 319 (2020): 106800.

131. K. Palosaari and O. Tervonen, “Post-Processing Water-Fat Imaging Technique for Fat Suppression in a Low-Field MR Imaging System, Evaluation in Patients With Rheumatoid Arthritis,” *Magnetic Resonance Materials in Physics, Biology and Medicine* 15 (2002): 1–9.

132. E. Anoardo and G. G. Rodriguez, “New Challenges and Opportunities for Low-Field MRI,” *Journal of Magnetic Resonance Open* 14 (2023): 100086.

Supporting Information

Additional supporting information can be found online in the Supporting Information section. **Table S1:** Summary of learning-based denoising methods in low-field MRI. **Table S2:** Summary of super-resolution in low-field MRI using deep learning–based methods.